JEM Journal of Experimental Medicine

ARTICLE

Mouse model of SARS-CoV-2 reveals inflammatory role of type I interferon signaling

Benjamin Israelow[1,2*], Eric Song[1*], Tianyang Mao[1], Peiwen Lu[1], Amit Meir[3], Feimei Liu[1], Mia Madel Alfajaro[1,4], Jin Wei[1,4], Huiping Dong[1], Robert J. Homer[5], Aaron Ring[1], Craig B. Wilen[1,4], and Akiko Iwasaki[1,6]

Severe acute respiratory syndrome–coronavirus 2 (SARS-Cov-2) has caused over 13,000,000 cases of coronavirus disease (COVID-19) with a significant fatality rate. Laboratory mice have been the stalwart of therapeutic and vaccine development; however, they do not support infection by SARS-CoV-2 due to the virus's inability to use the mouse orthologue of its human entry receptor angiotensin-converting enzyme 2 (hACE2). While hACE2 transgenic mice support infection and pathogenesis, these mice are currently limited in availability and are restricted to a single genetic background. Here we report the development of a mouse model of SARS-CoV-2 based on adeno-associated virus (AAV)–mediated expression of hACE2. These mice support viral replication and exhibit pathological findings found in COVID-19 patients. Moreover, we show that type I interferons do not control SARS-CoV-2 replication in vivo but are significant drivers of pathological responses. Thus, the AAV-hACE2 mouse model enables rapid deployment for in-depth analysis following robust SARS-CoV-2 infection with authentic patient-derived virus in mice of diverse genetic backgrounds.

Introduction

In the first few months of 2020, severe acute respiratory syndrome–coronavirus 2 (SARS-Cov-2) has caused millions of cases of coronavirus disease (COVID-19), becoming a global pandemic with overall case fatality rates around 1–2%, but as high as 15–20% in older and higher comorbidity demographics (Dong et al., 2020; Wang et al., 2020; Zhu et al., 2020). While sporadic outbreaks of highly virulent coronaviruses including Middle Eastern respiratory syndrome coronavirus (MERS-CoV) and severe acute respiratory syndrome–coronavirus (SARS-CoV) remained relatively self-contained, SARS-CoV-2 spread rapidly throughout the world, indicating a clear difference in patterns of viral transmission, control, and pathogenesis (Dong et al., 2020). Due to the urgency of this global pandemic, numerous therapeutic and vaccine trials have begun without customary safety and efficacy studies (Callaway, 2020). The development of animal models that support SARS-CoV-2 infection and recapitulate COVID-19 are urgently needed to study critical aspects of viral infection, replication, pathogenesis, and transmission, and more importantly, to support therapeutic testing and identify vaccine candidates. While multiple animal models have been proposed, such as the Syrian golden hamster (Sia et al., 2020), ferret (Blanco-Melo et al., 2020), and nonhuman primates (Rockx et al., 2020), none of these provide the tools necessary for in-depth analysis that mice provide.

Mice are the most widely used animal model in laboratory research due to their small size, fast reproduction time, and low maintenance costs. Unfortunately, they do not support infection by SARS-CoV-2 due to the virus's inability to use the mouse orthologue of its human entry receptor angiotensin-converting enzyme 2 (hACE2; Letko et al., 2020). Despite also using the hACE2 receptor for cell entry, SARS-CoV could infect mice, causing only mild disease. Mouse-adapted SARS-CoV was developed by multiple laboratories to more closely model SARS-COV human disease (Day et al., 2009; Roberts et al., 2007). This advance enabled more in-depth study of immune correlates of pathogenesis and protection, including the discovery that type I IFN signaling was pathogenic in the setting of SARS-CoV challenge (Channappanavar et al., 2016). This correlated with fatal human cases, which showed robust expression of type I IFN (Cameron et al., 2007). The first mouse model to support MERS-CoV infection used mice transduced with an adenoviral vector to express dipeptidyl peptidase-4, the MERS-CoV receptor, which

[1]Department of Immunobiology, Yale University School of Medicine, New Haven, CT; [2]Department of Internal Medicine, Section of Infectious Diseases, Yale University School of Medicine, New Haven, CT; [3]Department of Microbial Pathogenesis, Yale University School of Medicine, New Haven, CT; [4]Department of Laboratory Medicine, Yale University School of Medicine, New Haven, CT; [5]Department of Pathology, Yale University School of Medicine, New Haven, CT; [6]Howard Hughes Medical Institute, Chevy Chase, MD.

*B. Israelow and E. Song contributed equally to this paper; Correspondence to Akiko Iwasaki: akiko.iwasaki@yale.edu.

interestingly led to the discovery that type I IFN signaling was protective rather than pathogenic in MERS-CoV infection (Zhao et al., 2014). Type I IFN signaling is clearly important in protecting against viral infections (tenOever, 2016), as well as the development of adaptive immunity (Iwasaki and Medzhitov, 2010). However, overactive or unregulated IFN signaling causes pathology in many viral infections (Cameron et al., 2007; Channappanavar et al., 2016; Davidson et al., 2014; Pillai et al., 2016; Yockey et al., 2018), bacterial infections (Boxx and Cheng, 2016), and autoimmune diseases (Crow et al., 2019).

Bao et al. (2020) recently published the repurposing of hACE2 transgenic mice (developed for the study of SARS-CoV), which were shown to support infection and pathogenesis by SARS-CoV-2. While these mice will provide much a much-needed tool for the study of SARS-CoV-2, these mice are currently limited in availability and are restricted to a single genetic background. Here we report the development of a mouse model of SARS-CoV-2 based on adeno-associated virus (AAV)–mediated expression of hACE2. These mice support viral replication and antibody production and exhibit pathological findings found in COVID-19 patients. Moreover, we show that type I IFNs only minimally control SARS-CoV-2 replication, but are significant drivers of pathological responses. Thus, the AAV-hACE2 mouse model enables rapid deployment for in-depth analysis following robust SARS-CoV-2 infection with authentic patient-derived virus in mice of diverse genetic backgrounds. This represents a much-needed platform for rapidly testing prophylactic and therapeutic strategies to combat COVID-19.

Results

Development of SARS-CoV-2 mouse model

To overcome the limitation that mouse ACE2 does not support SARS-CoV-2 cellular entry and infection (Hoffmann et al., 2020; Letko et al., 2020), we developed a mouse model of SARS-CoV-2 infection and pathogenesis by delivering hACE2 into the respiratory tract of C57BL/6J (B6J) mice via AAV9 (Fig. 1 a). Control (AAV-GFP or mock transduced) and AAV-hACE2 mice were intranasally infected with 10^6 PFU SARS-CoV-2 (passage 2 of isolate USA-WA1/2020). Mice were sacrificed at 2, 4, 7, and 14 d post-infection (DPI). During the 14-d time course, mice were monitored daily for weight loss. None developed significant weight changes or died. Compared with control, AAV-hACE2 mice supported productive infection indicated by a >200-fold increase in SARS-CoV-2 RNA (Fig. 1 b) as well as the presence of infectious virus as indicated by plaque assay (Fig. 1 c).

We next performed histopathologic examination of lung sections from 2 and 4 DPI. We found mild diffuse peribronchial infiltrates in AAV-hACE2 mice, which was minimal in control mice (Fig. 1, e and f). Immunofluorescence staining (Fig. 1 d) of lung sections revealed diffuse infection (SARS-CoV-2 N protein/red) within alveolar epithelia (EpCAM/green). Similar to findings in COVID-19 patients (Liao et al., 2020), we found an expansion of pulmonary infiltrating myeloid-derived inflammatory cells characterized by early $Ly6C^{hi}$ monocytes and inflammatory monocyte-derived macrophages ($CD64^+CD11c^-CD11b^+Ly6C^+$; Fig. 1 g; Fig. S1, d and e; and Fig. S2 d). Additionally, we observed relative increases of activated lymphoid cells in lung tissue, including increased percentages of $CD69^+$ (recent activation) and $CD44^+$ (recent antigen exposure) $CD4^+$ and $CD8^+$ T cells (Fig. 1 g; Fig. S1, b and c; and Fig. S3 c). Last, the population of activated ($CD69^+$) natural killer (NK) cells expanded during early infection as well.

The role of adaptive immunity and, specifically, antibody response to SARS-CoV-2 is particularly important in the development of safe and effective vaccines. To assess the capacity for B6J AAV-hACE2 mice to mount an antibody response to SARS-CoV-2 challenge, we quantified anti-spike protein IgG titers by ELISA (Amanat et al., 2020; Stadlbauer et al., 2020). We found that while control-infected mice did not develop anti-spike antibodies, AAV-hACE2 B6/J mice mounted a significant antibody response between 4 and 7 DPI, which continued to increase at 14 DPI (Fig. 1 h). Next, to assess the neutralization potential of these antibodies, we performed plaque reduction neutralization assay (PRNT) using SARS-CoV-2, and found $PRNT_{75}$ at a serum dilution of 1:1,024 as early as 7 DPI (Fig. 1 i).

IFN-stimulated genes and inflammatory cytokines are acutely up-regulated during SARS-CoV-2 infection

In a recent study, Blanco-Melo et al. (2020) showed cytokine signatures that are out of proportion to the IFN response in autopsy samples from COVID-19 patients, infected ferrets, and SARS-CoV-2–infected cells in culture. However, others have reported elevated IFN signatures in the lungs of COVID-19 patients (Zhou et al., 2020). The discrepancy between these studies may reflect differential timing of sampling and severity of disease. To assess both the cytokine and IFN response to SARS-CoV-2–infected AAV-hACE2 mice, we performed RNA sequencing from infected lung at 2 DPI. In contrast to the control-infected mice, AAV-hACE2 mice developed clear signatures of cytokines and IFN-stimulated genes (ISGs). In fact, the majority of the differentially expressed up-regulated genes were either ISGs or cytokines (Fig. 2 a). Interestingly, type I, type II, and type III IFN did not seem to be up-regulated. Using the Interferome database (http://www.interferome.org/), we mapped the top up-regulated genes to their transcriptional regulation by type I, II, or III IFNs (Fig. 2 b). We found that while most of the genes shared regulation by type I and type II (and some by all three IFNs), a distinct subset of 45 genes that were specific to type I IFN signaling was elevated in the infected lung. We next performed gene ontology analysis of the top up-regulated genes, which revealed enrichment of gene clusters in virus–host interaction, immune response, and immune cell recruitment and activation (Fig. 2 c), consistent with the proinflammatory immune cell infiltrates seen in patients. To analyze the concordance between our model and the recently published patient lung autopsy gene expression from Blanco-Melo et al. (2020), we found that 73% of our shared up-regulated genes were ISGs (Fig. 2, d and e). These results indicated that our mouse model largely recapitulated the transcriptome changes observed in the lungs of COVID-19 patients.

Type I IFN signaling is required for recruitment of proinflammatory cells into the lungs and ISG expression, but not for viral clearance

To further investigate the role of type I IFN signaling in SARS-CoV-2 infection, we transduced IFN-α receptor–deficient B6/J mice ($IFNAR^{-/-}$) and IFN regulatory transcription factor 3/7 double

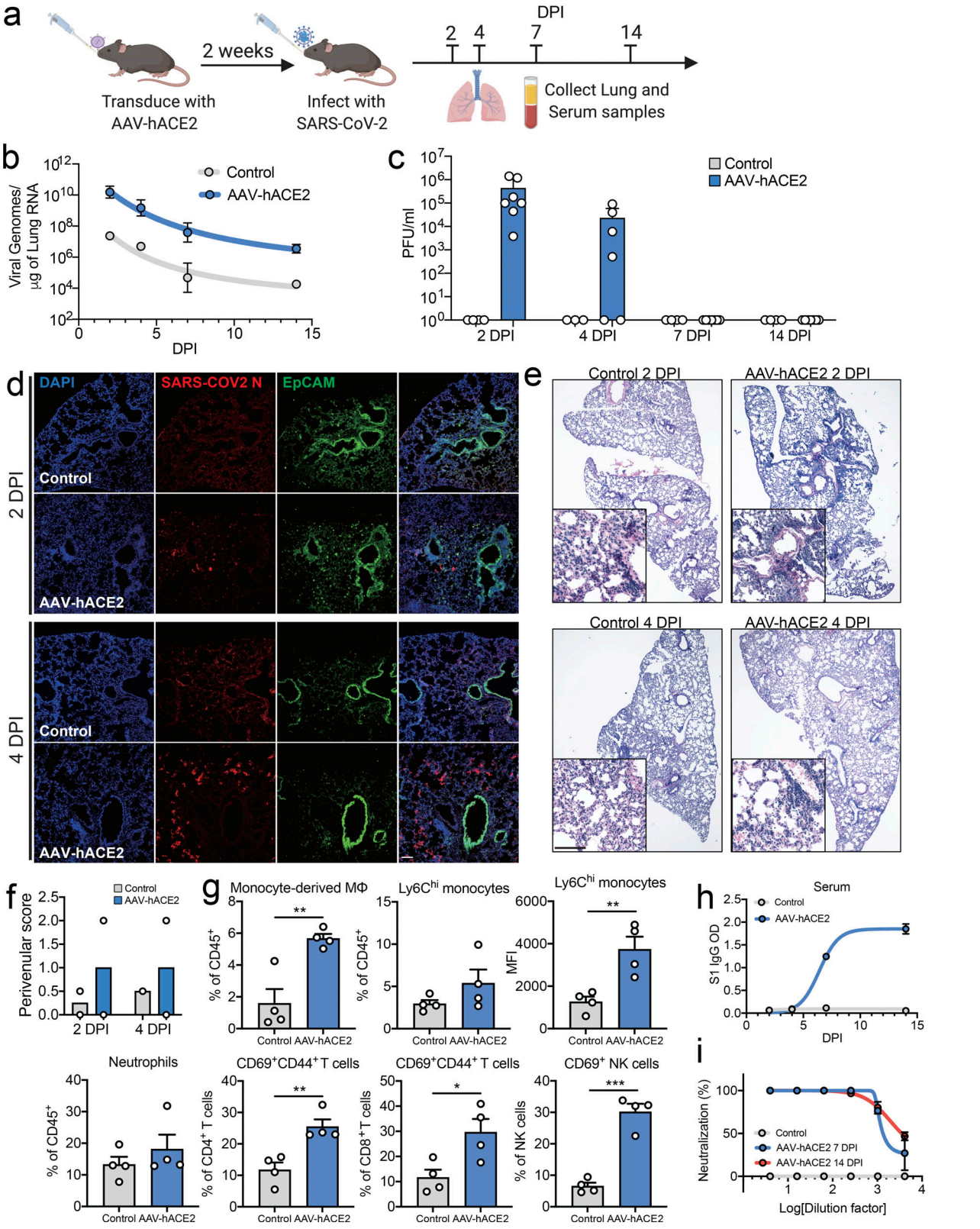

Figure 1. **AAV-hACE2 transduction allows for productive SARS-CoV-2 infection in vivo. (a)** Schematic of experimental plans. C57BL/6J mice were transduced intratracheally with an AAV coding for hACE2 (AAV-hACE2) or control (AAV-GFP or PBS) and infected with SARS-CoV-2 2 wk after. Lung and blood samples were collected at days 2, 4, 7, and 14 for analysis. **(b)** Viral RNA from lung homogenates were measured using quantitative PCR against SARS-CoV-2. **(c)** Viral titers from lung homogenates were performed by plaque assay on VeroE6 cells (AAV-hACE2 values noted as mean ± SEM from three independent experiments; *n* = 7 at 2 and 14 DPI; *n* = 6 at 4 and 7 DPI. Control values noted as mean ± SEM from two independent experiments; *n* = 4 at 2, 7, and 14 DPI; *n* = 3 at 4 DPI). **(d)** Frozen lung tissue was stained for SARS-CoV-2 N protein (red) and epithelial cells (EpCAM, green). **(e)** Fixed lung tissue was paraffin-embedded

and stained with H&E. Magnified panels highlight leukocyte infiltration and perivenular inflammation. **(f)** Images from panel e were scored by a pulmonary pathologist for perivenular inflammation (n = 2). **(g)** At 2 DPI, single-cell suspensions of lung were analyzed by flow cytometry. Data are shown as frequency of $CD45^+$ cells (monocyte-derived macrophages, Ly6Chi monocytes, and neutrophils), frequency of parent cells ($CD44^+CD69^+CD4^+$ T cells, $CD44^+CD69^+CD8^+$ T cells, and $CD69^+$ NK cells), or mean fluorescence intensity of CD64 (Ly6Chi monocytes; AAV-hACE2 and control values noted as mean ± SEM from two independent experiments, n = 4). **(h)** Serum antibodies were measured against spike protein using an ELISA. **(i)** Day 7 and 14 sera from panel h were used to perform a PRNT on VeroE6 cells incubated with SARS-CoV-2 (AAV-hACE2 noted as mean ± SEM from two independent experiments, n = 4; control value, n = 1). P values were calculated by two-tailed unpaired Student's t test. *, P < 0.05; **, P < 0.01; ***, P < 0.005. Scale bars, 100 µm.

knockout B6/J mice ($IRF3/7^{-/-}$), two key transcription factors needed to induce IFNs and ISGs (Honda et al., 2006), with AAV-hACE2 and infected them intranasally with 10^6 PFU SARS-CoV-2.

We found no significant difference in either viral RNA or viral titer between $IFNAR^{-/-}$, $IRF3/7^{-/-}$, and WT B6/J AAV-hACE2–infected mice (Fig. 3, a and b). While viral infection was not significantly altered in either $IFNAR^{-/-}$ or $IRF3/7^{-/-}$ mice, we found a significant loss of recruitment of inflammatory cells to their lungs. Recruitment of $Ly6C^{hi}$ monocytes and monocyte-derived macrophages to the lungs of mice deficient in IFNAR or IRF3/7 was significantly reduced (Fig. 3, d and e; and Fig. S2 c). Additionally, we found reduced activation of $CD4^+$ and $CD8^+$ cells in $IRF3/7^{-/-}$-infected mice, and a complete loss of activation of these cell populations in $IFNAR^{-/-}$-infected mice (Fig. 3, f–h; and Fig. S3 a). In contrast, we observed robust recruitment of neutrophils in the infected $IFNAR^{-/-}$ mice (Fig. 3 i), which may reflect the loss of IFN-mediated neutrophil regulation and regulation of inflammasomes (Galani et al., 2017; Metzemaekers et al., 2018; Seo et al., 2011). These results were consistent with previous reports of pulmonary type I IFN signaling representing a major driver of both recruitment and activation of proinflammatory immune cells in viral infections including SARS-CoV (Channappanavar et al., 2016) and other respiratory viral infections (Makris et al., 2017). RNA sequencing (RNA-seq) at 2 DPI from the lungs of infected WT, $IFNAR^{-/-}$, and $IRF3/7^{-/-}$ mice reveal markedly elevated ISGs, cytokines, and chemokines in WT mice that were absent in $IFNAR^{-/-}$ and $IRF3/7^{-/-}$. Heat map analysis of the top 100 up-regulated genes showed significant elevation of antiviral ISGs (Rsad2, IRF7, OASL, Ifit, STAT2, and MX2) as well as monocyte recruiting chemokines (Cxcl10, Ccl7, and Ccl2), which were not up-regulated in either $IFNAR^{-/-}$- or $IRF3/7^{-/-}$-infected mice (Fig. 3 c).

Discussion

In this study, we describe the development of a mouse model of SARS-CoV-2 using AAV-hACE2 delivery to the mouse respiratory tract. This model develops productive SARS-CoV-2 infection as well as inflammatory pulmonary infiltrates that are characteristic of COVID-19 in humans. We found an acute inflammatory immune response characterized by infiltrating monocytes, macrophages, and neutrophils, as well as activated T and NK cells. We also found gene signatures of acute ISG response, which clusters most closely with type I IFN response. In addition to the acute inflammatory response, these mice develop rapid SARS-CoV-2 S-specific IgG and neutralizing antibodies around 7 DPI. While none of the mice exhibited infection-related mortality, this may reflect the immune status of the challenged mice, which were 6–12-wk-old healthy adult mice. Future studies in aged, immunocompromised, and/or obese mice may elicit more dramatic phenotypes, similar to the effect of these comorbidities in human COVID-19 disease.

To better understand the role of type I IFN signaling during SARS-CoV-2, we infected both $IFNAR^{-/-}$ and $IRF3/7^{-/-}$ and showed that there were minimal differences in the viral replication and viral persistence between $IFNAR^{-/-}$, WT, and $IRF3/7^{-/-}$. This was in spite of a robust ISG response in WT mice lungs, which was absent in $IFNAR^{-/-}$ and $IRF3/7^{-/-}$ mice. Furthermore, viral clearance was not significantly augmented by the lack of IFN signaling, suggesting that endogenous IFN signaling is not sufficient for clearance of SARS-CoV-2 infection. Interestingly, despite high levels of ISGs, we did not find high levels of IFNs, which was similar to postmortem lung samples from COVID-19 patients (Blanco-Melo et al., 2020).

While endogenous type I IFN signaling is unable to shut down SARS-CoV-2 replication in our model, possibly due to its vast array of IFN antagonists (Park and Iwasaki, 2020), we found that it clearly orchestrates a proinflammatory immune response characterized by the recruitment of proinflammatory monocytes and macrophages as well as the activation of $CD4^+$, $CD8^+$, and NK cells, which likely contributes to immunopathology in patients (Liao et al., 2020). Similar to our findings, $STAT2^{-/-}$ hamsters infected with SARS-CoV-2 were shown to develop less lung pathology than WT hamsters (Boudewijns et al., 2020 *Preprint*). Despite the use of type I IFN in the treatment of both MERS and SARS-CoV, its endogenous role is less clear with reports of protective effects for MERS (Zhao et al., 2014), and pathogenic effects for SARS-CoV (Cameron et al., 2007; Channappanavar et al., 2016). Notably, overactive or unregulated IFN signaling causes pathology in other viral infections including influenza (Davidson et al., 2014; Pillai et al., 2016) and congenital Zika (Yockey et al., 2018). The role of type I IFN signaling in SARS-CoV-2 and COVID-19 is critically important to understanding the protection provided by both the innate and adaptive arms of the immune system and to elucidate any pathogenic effects. These data are especially concerning given current use of type I IFN as a therapeutic for the treatment of COVID-19. Our results indicate a potential pathological role of endogenous type I IFN in COVID-19 respiratory inflammation.

Here we present clear evidence of both the inadequate antiviral activity as well as the potential harms of endogenous type I IFN responses. To our knowledge, this is the first report that AAV-based hACE2 delivery to the mouse respiratory tract is sufficient to enable robust SARS-CoV-2 infection. During the preparation of this manuscript, two publications (Bao et al., 2020; Jiang et al., 2020) reported SARS-CoV-2 infection and pathogenesis in different transgenic hACE2-expressing mice. Additionally, infectious models in hamsters (Sia et al., 2020),

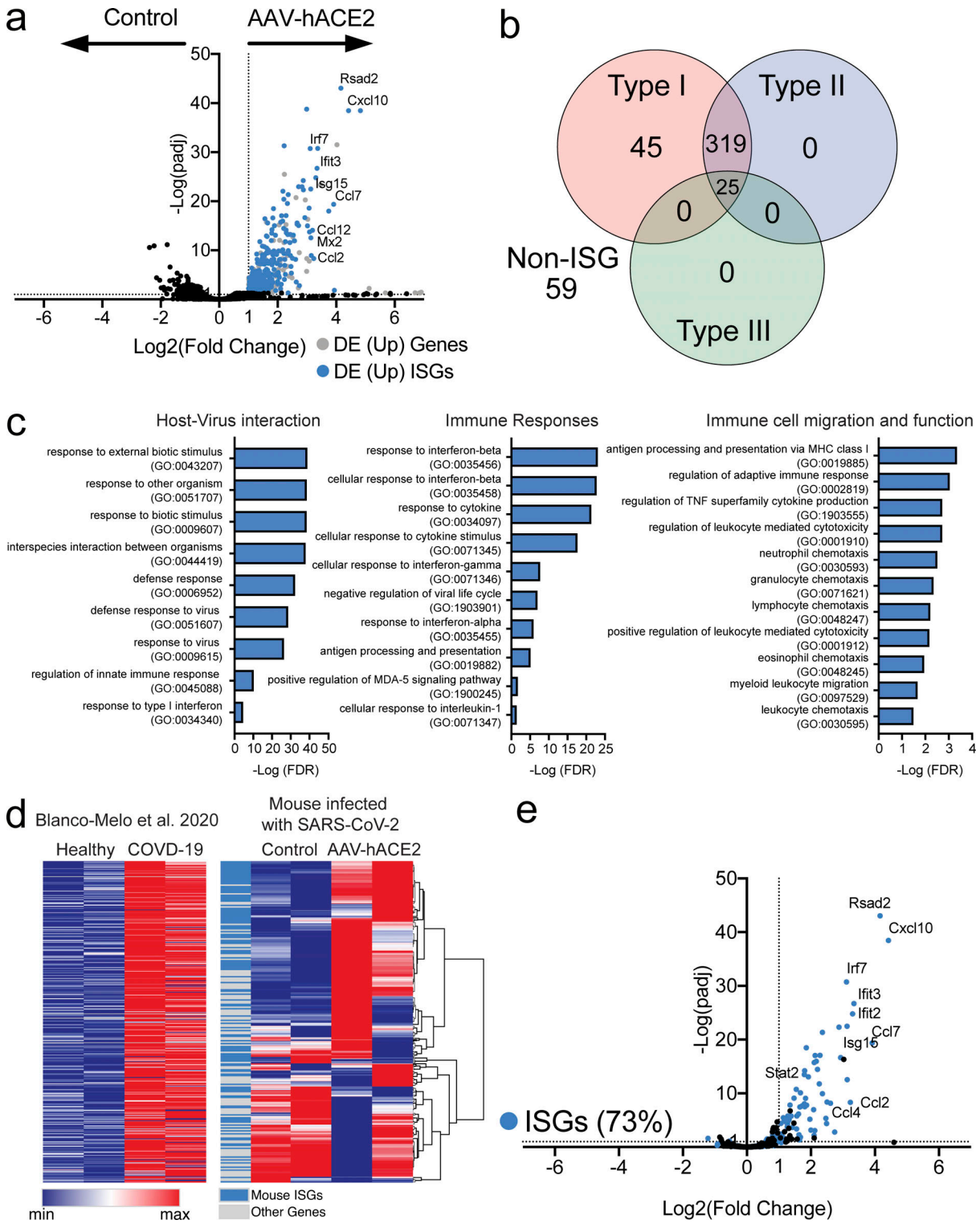

Figure 2. **AAV-hACE2 mice infected with SARS-CoV-2 show similar IFN signatures as COVID-19 patients. (a)** Volcano plot showing differential expression (DE) of genes from whole lungs of mice infected with SARS-CoV-2 with and without AAV-hACE2 at 2 DPI. Gray indicates significantly differentially up-regulated genes, and blue indicates subsets of genes that are known ISGs. **(b)** Significantly up-regulated genes were put into Interferome (https://www.interferome.org) to identify how many genes are stimulated by type I, type II, or type III IFNs. **(c)** Gene Ontology Enrichment Analysis was performed on significantly up-regulated genes to identify enriched cellular processes. **(d)** Up-regulated gene list from human samples (Blanco-Melo et al., 2020) was graphed (left panel) and used to perform hierarchical clustering for differentially expressed genes from lungs of AAV-hACE2 SARS-CoV-2–infected mice (blue, mouse ISGs; gray, other genes). **(e)** Subset of differentially expressed genes in panel a that were significantly up-regulated in lungs of COVID-19 patients (from Blanco-Melo et al., 2020).

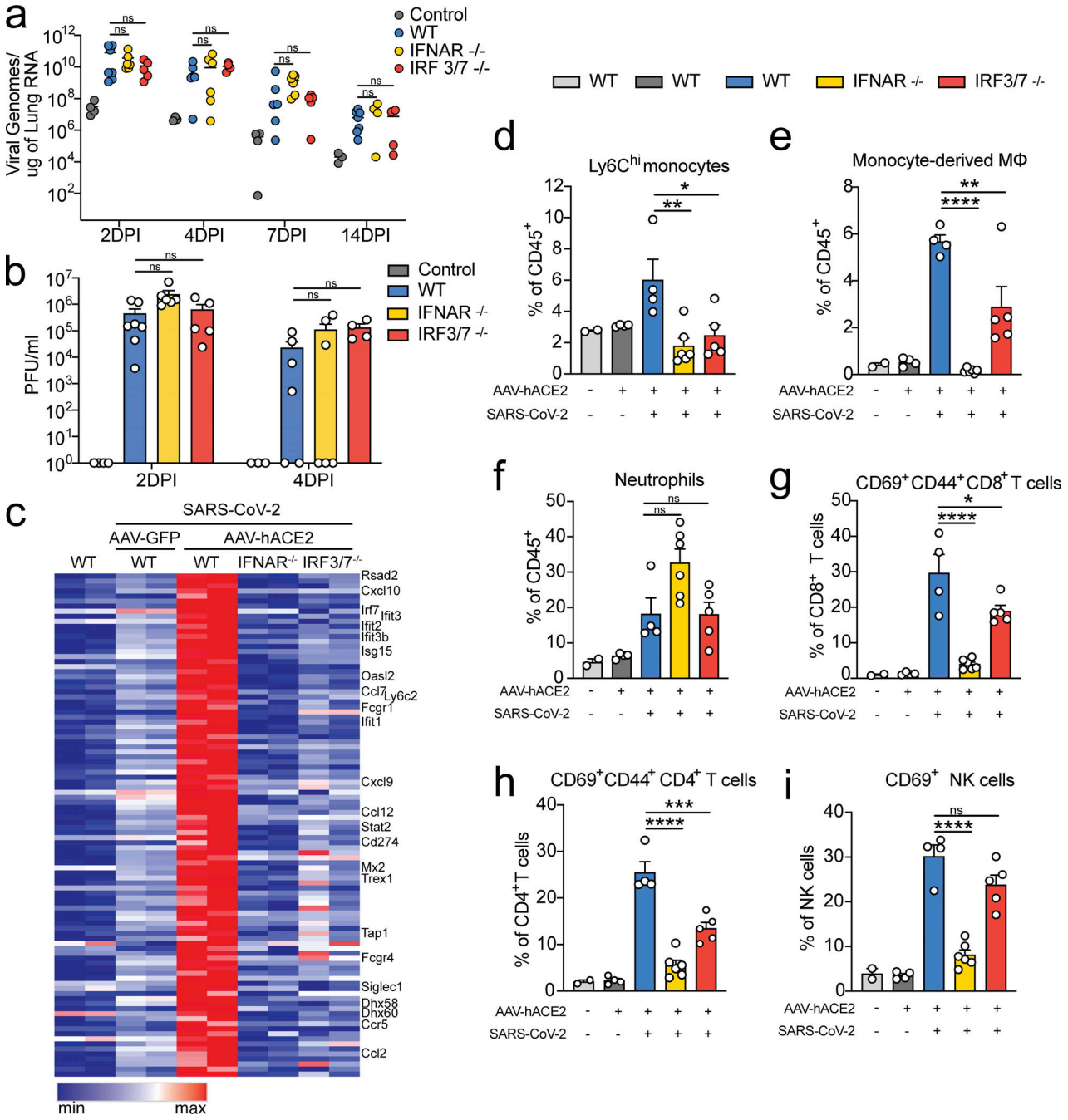

Figure 3. **AAV-hACE2 mice infected with SARS-CoV-2 exhibit type I IFN-dependent immune cell infiltration.** C57BL/6J (WT), IFNAR knockout, and IRF3/7 double knockout mice were transduced intratracheally with an AAV encoding hACE2 (AAV-hACE2) and infected with SARS-CoV-2 2 wk later. **(a)** Viral titers in the lungs of mice were measured using quantitative PCR against SARS-CoV-2. **(b)** Lung homogenates titered on VeroE6 cells (control and WT were from the same experiment as Fig. 1; IFNAR$^{-/-}$ values from three independent experiments, n = 6 at 2, 4, and 7 DPI, and n = 4 at 14 DPI; IRF3/7$^{-/-}$ values from two independent experiments, n = 5 at 2 and 7 DPI, and n = 4 at 4 and 14 DPI). **(c)** Heat map of top 100 up-regulated genes in SARS-CoV-2–infected C57BL/6J (WT) mice transduced with AAV-hACE2 versus SARS-CoV-2–infected AAV-GFP–transduced mice. Relative expression of these genes in noninfected/nontransduced mice and IFNAR$^{-/-}$ and IRF3/7$^{-/-}$ AAV-hACE2–transduced and SARS-CoV-2–infected mice. **(d–i)** At 2 DPI, lungs of mice were made into single-cell suspensions for flow cytometry (WT [light gray] nontransduced, noninfected values from single experiment, n = 2; WT [dark gray] AAV-hACE2 and not infected values from two independent experiments, n = 4; WT [blue] AAV-hACE2 and infected values from two independent experiments, n = 4; IFNAR$^{-/-}$ values from three independent experiments, n = 6; and IRF3/7$^{-/-}$ values from two independent experiments, n = 5). P values were calculated by one-way ANOVA with Tukey's multiple comparison test. *, P < 0.05; **, P < 0.01; ***, P < 0.005; ****, P < 0.001. ns, not significant.

ferrets (Blanco-Melo et al., 2020), and nonhuman primates (Rockx et al., 2020) have also been reported. These models are valuable and have provided much-needed tools for the study of SARS-CoV-2 disease. The uniqueness of the AAV-hACE2 model is the ability to test SARS-CoV-2 in diverse genetic background mice in a relatively short time. Our mouse model provides a powerful tool to perform detailed investigation of SARS-CoV-2 pathogenesis and dissect the correlates of protection owing to existence of a variety of genetic knockouts and flow cytometry reagents. This strategy not only allows us to quickly identify key factors in anti–SARS-CoV-2 immunity, but also reduces costs associated with mouse breeding and time. Supporting this model, during the revision of this manuscript, two publications reported that delivery of hACE2 via adenovirus (AdV)-based vector to mice led to productive infection and disease (Hassan et al., 2020; Sun et al., 2020). The major advantage of using AAV rather than AdV is that AAV has significantly less immunogenicity (Jooss and Chirmule, 2003), which is a critical factor to consider when studying immune responses during viral infections. It is certainly possible that this difference in model underlies differences in replication between our study and that reported in Sun et al. (2020); however, protection from immunopathology in IFNAR$^{-/-}$ is consistent in both studies. In addition, AAV has significantly longer expression kinetics compared with AdV, months compared with days, which allows for a wider possibility of experimental procedures, such as studying duration of adaptive immunity. Thus, the AAV-hACE2 mouse model described here offers a broadly available and highly adaptable animal model to understand critical aspects of SARS-CoV-2 viral infection, replication, pathogenesis, and protection, with authentic patient-derived virus. This model provides a vital platform for testing prophylactic and therapeutic strategies to combat COVID-19.

Materials and methods

All procedures were performed in a BSL-3 facility (for SARS-CoV-2–infected mice) with approval from the Yale Institutional Animal Care and Use Committee and Yale Environmental Health and Safety.

Mice

6- to 12-wk-old mixed sex C57Bl/6 (B6J) and B6(Cg)-*Ifnar1*$^{tm1.2Ees}$/J (*Ifnar1*$^{-/-}$) purchased from Jackson Laboratories, and IRF3/7$^{-/-}$ (generous gift from T. Taniguchi; University of Tokyo, Tokyo, Japan), and were subsequently bred and housed at Yale University. All procedures used in this study (sex-matched, age-matched) complied with federal guidelines and the institutional policies of the Yale School of Medicine Animal Care and Use Committee.

Antibodies

Anti-I-A/I-E (M5/114.15.2, Pacific blue, B211129, 107620), anti-CD45 (30-F11, BV605, B283182, 103155), anti-CD11c (N418, BV711, B265348, 117349), anti-CD45R/B220 (RA3-6B2, FITC, B230445, 103206), anti-Ly-6C (HK1.4, PerCP/Cy5.5, B250461, 128011), anti-CD64 (X54-5/7.1, PE, B270364, 139304), anti-Ly6G (1A8, PE/Cy7, B194432, 127618), anti-Siglec-F (E50-2440, A647, 3214986, 562680), anti-CD11b (M1/70, A700, B259438, 101222), anti-CD24 (M1/69, APCFire750, B292373, 101840), anti-CD45.2 (104, Pacific blue, B279653, 109820), anti-CD4 (RM4-5, BV605, B284681, 100548), anti-CD8 (53–6.7, BV711, B293230, 100759), anti-CD44 (IM7, FITC, B278352, 103006), anti-CD62L (MEL-14, PERCP5.5, B272105, 104432), anti-NK1.1 (PK136, PE, B221273, 108708), anti-CD69 (H1.2F3, PE/Cy7, B253212, 104512), and anti-CD3 (17A2, APC/Cyanine7, B283940, 100222) antibodies were purchased from BioLegend (as noted above by catalog numbers beginning with B) or BD Biosciences (as noted above by catalog numbers that do not begin with B).

AAV infection

AAV9 encoding hACE2 was purchased from Vector Biolabs (AAV-CMV-hACE2). Animals were anaesthetized using a mixture of ketamine (50 mg/kg) and xylazine (5 mg/kg), injected intraperitoneally. The rostral neck was shaved and disinfected. A 5-mm incision was made, the salivary glands were retracted, and the trachea was visualized. Using a 32-G insulin syringe, a 50-µl bolus injection of 10^{11} genomic copies per milliliter of AAV-CMV-hACE2 or control (AAV-GFP or PBS) was injected into the trachea. The incision was closed with 4–0 Vicryl suture. Following intramuscular administration of analgesic (meloxicam and buprenorphine, 1 mg/kg), animals were placed in a heated cage until full recovery.

Generation of SARS-CoV-2 stocks

To generate SARS-CoV-2 viral stocks, Huh7.5 cells were inoculated with SARS-CoV-2 isolate USA-WA1/2020 (NR-52281; BEI Resources) to generate a P1 stock. To generate a working VeroE6, cells were infected at an MOI 0.01 for 4 d to generate a working stock. Supernatant was clarified by centrifugation (450 *g* × 5 min) and filtered through a 0.45-µm filter. To concentrate virus, one volume of cold (4°C) 4× PEG-it Virus Precipitation Solution (40% [wt/vol] PEG-8000 and 1.2 M NaCl) was added to three volumes of virus-containing supernatant. The solution was mixed by inverting the tubes several times and then incubated at 4°C overnight. The precipitated virus was harvested by centrifugation at 1,500 *g* for 60 min at 4°C. The pelleted virus was resuspended in PBS and then aliquoted for storage at −80°C. Virus titer was determined by plaque assay using Vero E6 cells.

SARS-CoV-2 infection

Mice were anesthetized using 30% vol/vol isoflurane diluted in propylene glycol. Using a pipette, 50 µl of SARS-CoV-2 (3×10^7 PFU/ml) was delivered intranasally.

Viral RNA analysis

At indicated time points, mice were euthanized in 100% isoflurane. Approximately 33% of total lung was placed in a bead homogenizer tube with 1 ml of PBS + 2% FBS. After homogenization, 250 µl of this mixture was placed in 750 µl Trizol LS (Invitrogen), and RNA was extracted with the RNeasy mini kit (Qiagen) per the manufacturer's protocol. To quantify SARS-CoV-2 RNA levels, we used the Luna Universal Probe Onestep RT-qPCR Kit (New England Biolabs) with 1 µg of RNA, using the US Centers for Disease Control and Prevention real-time RT-PCR primer/probe sets for 2019-nCoV_N1.

Viral titer

Lung homogenates were cleared of debris by centrifugation (3,900 *g* for 10 min). Infectious titers of SARS-CoV-2 were determined by plaque assay in Vero E6 cells in MEM supplemented with $NaHCO_3$, 4% FBS, and 0.6% Avicel RC-581. Plaques were resolved at 48 h after infection by fixing in 10% formaldehyde for 1 h followed by staining for 1 h in 0.5% crystal violet in 20% ethanol. Plates were rinsed in water to visualize plaques.

PRNT assay

Serum samples were heat-inactivated by incubation at 56°C for 30 min before use. Mouse plasma was serially fourfold diluted from 1:4 to 1:4,096, and then an equal volume of SARS-CoV-2 virus was added (~30 PFU) and incubated at 37°C for 30 min. After incubation, 100-µl mixtures were inoculated onto monolayer Vero E6 cells in a 12-well plate for 1 h. Cells were overlaid with MEM-supplemented $NaHCO_3$, 4% FBS, 0.6% Avicel mixture. Plaques were resolved at 48 h after infection by fixing in 10% formaldehyde for 1 h followed by staining for 1 h in 0.5% crystal violet.

Immunofluorescence microscopy

Tissue was collected and fixed in 4% paraformaldehyde overnight. Samples were then dehydrated in a 30% sucrose solution. Optimal cutting temperature compound–embedded 10-mm cryostat sections were blocked in 0.1 M Tris-HCl buffer with 0.3% Triton and 1% FBS before staining. Slides were stained for EpCAM (G8.8; Biolegend) with fluorochrome-labeled primary antibody. The primary antibodies rabbit anti-SARS-CoV-2 nucleocapsid (GeneTex) and rabbit anti-ACE2 (Abcam) or rabbit IgG isotype control were used and detected with secondary antibodies, donkey anti-rabbit IgG Alexa Fluor Plus 488/555 (Invitrogen). Slides were stained with DAPI (Sigma-Aldrich) and mounted with Prolong Gold Antifade reagent (Thermo Fisher Scientific). All slides were analyzed by fluorescence microscopy (BX51; Olympus) with a 10× lens. Imaging data were analyzed with Imaris 7.2 (Bitplane).

Immunohistochemistry

Yale pathology kindly provided assistance with embedding, sectioning and H&E staining of lung tissue. A pulmonary pathologist reviewed the slides blinded and identified immune cell infiltration and other related pathologies.

ELISA

ELISAs were performed as previously described (Amanat et al., 2020). In short, Triton X-100 and RNase A were added to serum samples at final concentrations of 0.5% and 0.5 mg/ml, respectively, and incubated at room temperature (RT) for 3 h before use to reduce risk from any potential virus in serum. 96-well MaxiSorp plates (442404; Thermo Fisher Scientific) were coated with 50 µl/well of recombinant SARS Cov-2 S1 protein (S1N-C52H3-100 µg; ACROBiosystems) at a concentration of 2 µg/ml in PBS and were incubated overnight at 4°C. The coating buffer was removed, and plates were incubated for 1 h at RT with 200 µl of blocking solution (PBS with 0.1% Tween-20, 3% milk powder). Serum was diluted 1:50 in dilution solution (PBS with 0.1% Tween-20, 1% milk powder), and 100 µl of diluted serum was added for 2 h at RT. Plates were washed three times with PBS with 0.1% Tween-20 and 50 µl of mouse IgG-specific secondary antibody (405306, 1:10,000; BioLegend) diluted in dilution solution added to each well. After 1 h of incubation at room temperature, plates were washed three times with PBS with 0.1% Tween-20. Plates were developed with 100 µl of TMB Substrate Reagent Set (555214; BD Biosciences), and the reaction was stopped after 15 min by the addition of 2 N sulfuric acid. Plates were then read at a wavelength of 450 nm and 570 nm.

Isolation of mononuclear cells and flow cytometry

Tissue was harvested and incubated in a digestion cocktail containing 1 mg/ml collagenase A (Roche) and 30 µg/ml DNase I (Sigma-Aldrich) in RPMI at 37°C for 45 min. Tissue was then filtered through a 70-µm filter. Cells were treated with ammonium-chloride-potassium buffer and resuspended in PBS with 1% BSA. At this point, cells were counted using an automated cell counter (Thermo Fisher Scientific). Mononuclear cells were incubated on ice with Fc block and Aqua cell viability dye for 20 min. After washing, primary antibody staining was performed on ice for 30 min. After washing with PBS, cells were fixed using 4% paraformaldehyde. Cell population data were acquired on an Attune NxT Flow Cytometer and analyzed using FlowJo Software (10.5.3; Tree Star).

RNA-seq

Libraries were made with the kind help of the Yale Center for Genomic Analysis. Briefly, libraries were prepared with an Illumina rRNA depletion kit and sequenced on a NovaSeq. RNA-seq data were aligned using STAR (STAR/2.5.3a-foss-2016b, mm10 assembly) with parameters --runThreadN 20 --outSAMtype BAM SortedByCoordinate --limitBAMsortRAM 35129075129 --outFilterMultimapNmax 1 --outFilterMismatchNmax 999 --outFilterMismatchNoverLmax 0.02 --alignIntronMin 20 --alignIntronMax 1000000 --alignMatesGapMax 1000000 for mapping of repetitive elements. Counts were counted using BEDTools (BEDTools/2.27.1-foss-2016b), coverageBed function, normalized using DESEQ2, and graphed using the Broad Institute Morpheus web tool. For IFN-stimulated gene identification, http://www.interferome.org was used with parameters -In Vivo, -*Mus musculus*, -fold change up 2 and down 2.

Statistical analysis

The data were analyzed by Student's *t* test or one-way ANOVA with Tukey's multiple comparison test. All statistical tests were calculated using GraphPad Prism (GraphPad software). A P value of <0.05 was considered statistically significant.

Graphical illustrations

Graphical illustrations were made with Biorender.com.

Data availability

The sequence reported in this paper has been deposited in the GenBank database (accession no. PRJNA646535).

Online supplemental material

Fig. S1 shows human ACE2 immunohistochemistry of mouse lungs transduced with AAV-hACE2; gating strategy for lymphoid cell populations; representative FACS plots related to

Fig. 1; lung macrophage populations; and SARS-CoV-2 S protein ELISA titration. Fig. S2 shows gating strategy for myeloid subsets; representative FACS plots related to Fig. 3, d and e; quantification of dendritic cell populations and eosinophils related to Fig. 3; and myeloid cell population kinetics related to Fig. 1 g. Fig. S3 shows representative FACS plots and quantification of parental lymphoid cell populations related to Fig. 3, g–i, as well as lymphoid cell population kinetics related to Fig. 1 g.

Acknowledgments

This study was supported by awards from National Institutes of Health grants 2T32AI007517-16 (to B. Israelow), T32GM007205 and F30CA239444 (to E. Song), R37AI041699 (to A. Meir), AI054359 and AI127429 (to A. Iwasaki), T32AI007019 (to T. Mao), and K08 AI128043 (to C.B. Wilen), as well as the Women's Health Research at Yale Pilot Project Program (A. Iwasaki and A. Ring), a Fast Grant from Emergent Ventures at the Mercatus Center (A. Iwasaki, E. Song, and C.B. Wilen), the G. Harold and Leila Y. Mathers Foundation (A. Ring, C.B. Wilen, and A. Iwasaki), and the Ludwig Family Foundation (A. Iwasaki, A. Ring, and C.B. Wilen). A. Iwasaki is an investigator of the Howard Hughes Medical Institute.

Author contributions: B. Israelow, E. Song, and A. Iwasaki planned the project. B. Israelow, E. Song, T. Mao, and A. Iwasaki designed, analyzed, and interpreted data. B. Israelow and A. Iwasaki wrote the manuscript. B. Israelow, E. Song, T. Mao, P. Lu, A. Meir, and F. Liu performed experiments and analyzed data. H. Dong bred and cared for animals. M.M. Alfajaro, J. Wei, R.J. Homer, A. Ring, and C.B. Wilen provided expertise, materials, and analysis of data.

Disclosures: A. Ring reported a patent to novel binding partner that interacts with SARS-CoV2 spike N-terminal domain pending; reports, "Unrelated to the subject of the work, I have founded, cofounded, and/or hold equity in biotechnology companies including Simcha Therapeutics, Forty Seven Inc., and ALX Oncology. I have also consulted for Medicenna Therapeutics, a company that licensed patents I invented in immuno-oncology. None of these companies are in the SARS-CoV-2 space or work on infectious disease to my knowledge. Broadly related to the subject of this work, within the past year, I have purchased and disposed shares in Gilead Sciences and Vir Biotechnology, which are working on therapeutics in the coronavirus space. I currently hold no shares in either of those companies." No other disclosures were reported.

Submitted: 15 June 2020
Revised: 15 July 2020
Accepted: 23 July 2020

References

Amanat, F., D. Stadlbauer, S. Strohmeier, T.H.O. Nguyen, V. Chromikova, M. McMahon, K. Jiang, G.A. Arunkumar, D. Jurczyszak, J. Polanco, et al. 2020. A serological assay to detect SARS-CoV-2 seroconversion in humans. *Nat. Med.* 26:1033–1036. https://doi.org/10.1038/s41591-020-0913-5

Bao, L., W. Deng, B. Huang, H. Gao, J. Liu, L. Ren, Q. Wei, P. Yu, Y. Xu, F. Qi, et al. 2020. The pathogenicity of SARS-CoV-2 in hACE2 transgenic mice. *Nature*. https://doi.org/10.1038/s41586-020-2312-y

Blanco-Melo, D., B.E. Nilsson-Payant, W.C. Liu, S. Uhl, D. Hoagland, R. Møller, T.X. Jordan, K. Oishi, M. Panis, D. Sachs, et al. 2020. Imbalanced Host Response to SARS-CoV-2 Drives Development of COVID-19. *Cell*. 181:1036–1045.e9. https://doi.org/10.1016/j.cell.2020.04.026

Boudewijns, R., H.J. Thibaut, S.J.F. Kaptein, R. Li, V. Vergote, L. Seldeslachts, C. De Keyzer, S. Sharma, S. Jansen, J.V. Weyenbergh, et al. 2020. STAT2 signaling as double-edged sword restricting viral dissemination but driving severe pneumonia in SARS-CoV-2 infected hamsters. *bioRxiv*. https://doi.org/10.1101/2020.04.23.056838 (Preprint posted July 2, 2020).

Boxx, G.M., and G. Cheng. 2016. The Roles of Type I Interferon in Bacterial Infection. *Cell Host Microbe*. 19:760–769. https://doi.org/10.1016/j.chom.2016.05.016

Callaway, E.. 2020. Coronavirus vaccines: five key questions as trials begin. *Nature*. 579:481. https://doi.org/10.1038/d41586-020-00798-8

Cameron, M.J., L. Ran, L. Xu, A. Danesh, J.F. Bermejo-Martin, C.M. Cameron, M.P. Muller, W.L. Gold, S.E. Richardson, S.M. Poutanen, et al; Canadian SARS Research Network. 2007. Interferon-mediated immunopathological events are associated with atypical innate and adaptive immune responses in patients with severe acute respiratory syndrome. *J. Virol.* 81:8692–8706. https://doi.org/10.1128/JVI.00527-07

Channappanavar, R., A.R. Fehr, R. Vijay, M. Mack, J. Zhao, D.K. Meyerholz, and S. Perlman. 2016. Dysregulated Type I Interferon and Inflammatory Monocyte-Macrophage Responses Cause Lethal Pneumonia in SARS-CoV-Infected Mice. *Cell Host Microbe*. 19:181–193. https://doi.org/10.1016/j.chom.2016.01.007

Crow, M.K., M. Olferiev, and K.A. Kirou. 2019. Type I Interferons in Autoimmune Disease. *Annu. Rev. Pathol.* 14:369–393. https://doi.org/10.1146/annurev-pathol-020117-043952

Davidson, S., S. Crotta, T.M. McCabe, and A. Wack. 2014. Pathogenic potential of interferon αβ in acute influenza infection. *Nat. Commun.* 5:3864. https://doi.org/10.1038/ncomms4864

Day, C.W., R. Baric, S.X. Cai, M. Frieman, Y. Kumaki, J.D. Morrey, D.F. Smee, and D.L. Barnard. 2009. A new mouse-adapted strain of SARS-CoV as a lethal model for evaluating antiviral agents in vitro and in vivo. *Virology*. 395:210–222. https://doi.org/10.1016/j.virol.2009.09.023

Dong, E., H. Du, and L. Gardner. 2020. An interactive web-based dashboard to track COVID-19 in real time. *Lancet Infect. Dis.* 20:533–534. https://doi.org/10.1016/S1473-3099(20)30120-1

Galani, I.E., V. Triantafyllia, E.E. Eleminiadou, O. Koltsida, A. Stavropoulos, M. Manioudaki, D. Thanos, S.E. Doyle, S.V. Kotenko, K. Thanopoulou, et al. 2017. Interferon-λ Mediates Non-redundant Front-Line Antiviral Protection against Influenza Virus Infection without Compromising Host Fitness. *Immunity*. 46:875–890.e6. https://doi.org/10.1016/j.immuni.2017.04.025

Hassan, A.O., J.B. Case, E.S. Winkler, L.B. Thackray, N.M. Kafai, A.L. Bailey, B.T. McCune, J.M. Fox, R.E. Chen, W.B. Alsoussi, et al. 2020. A SARS-CoV-2 infection model in mice demonstrates protection by neutralizing antibodies. *Cell*. S0092-8674(20)30742-X.

Hoffmann, M., H. Kleine-Weber, S. Schroeder, N. Krüger, T. Herrler, S. Erichsen, T.S. Schiergens, G. Herrler, N.H. Wu, A. Nitsche, et al. 2020. SARS-CoV-2 Cell Entry Depends on ACE2 and TMPRSS2 and Is Blocked by a Clinically Proven Protease Inhibitor. *Cell*. 181:271–280.e8. https://doi.org/10.1016/j.cell.2020.02.052

Honda, K., A. Takaoka, and T. Taniguchi. 2006. Type I interferon [corrected] gene induction by the interferon regulatory factor family of transcription factors. *Immunity*. 25:349–360. https://doi.org/10.1016/j.immuni.2006.08.009

Iwasaki, A., and R. Medzhitov. 2010. Regulation of adaptive immunity by the innate immune system. *Science*. 327:291–295. https://doi.org/10.1126/science.1183021

Jiang, R.-D., M.-Q. Liu, Y. Chen, C. Shan, Y.-W. Zhou, X.-R. Shen, Q. Li, L. Zhang, Y. Zhu, H.-R. Si, et al. 2020. Pathogenesis of SARS-CoV-2 in transgenic mice expressing human angiotensin-converting enzyme 2. *Cell*. 182:50–58.e8. https://doi.org/10.1016/j.cell.2020.05.027

Jooss, K., and N. Chirmule. 2003. Immunity to adenovirus and adeno-associated viral vectors: implications for gene therapy. *Gene Ther.* 10:955–963. https://doi.org/10.1038/sj.gt.3302037

Letko, M., A. Marzi, and V. Munster. 2020. Functional assessment of cell entry and receptor usage for SARS-CoV-2 and other lineage B betacoronaviruses. *Nat. Microbiol.* 5:562–569. https://doi.org/10.1038/s41564-020-0688-y

Liao, M., Y. Liu, J. Yuan, Y. Wen, G. Xu, J. Zhao, L. Cheng, J. Li, X. Wang, F. Wang, et al. 2020. Single-cell landscape of bronchoalveolar immune cells in patients with COVID-19. *Nat. Med.* 26:842–844. https://doi.org/10.1038/s41591-020-0901-9

Makris, S., M. Paulsen, and C. Johansson. 2017. Type I Interferons as Regulators of Lung Inflammation. *Front. Immunol.* 8:259. https://doi.org/10.3389/fimmu.2017.00259

Metzemaekers, M., V. Vanheule, R. Janssens, S. Struyf, and P. Proost. 2018. Overview of the Mechanisms that May Contribute to the Non-Redundant Activities of Interferon-Inducible CXC Chemokine Receptor 3 Ligands. *Front. Immunol.* 8:1970. https://doi.org/10.3389/fimmu.2017.01970

Park, A., and A. Iwasaki. 2020. Type I and Type III Interferons - Induction, Signaling, Evasion, and Application to Combat COVID-19. *Cell Host Microbe*. 27:870–878. https://doi.org/10.1016/j.chom.2020.05.008

Pillai, P.S., R.D. Molony, K. Martinod, H. Dong, I.K. Pang, M.C. Tal, A.G. Solis, P. Bielecki, S. Mohanty, M. Trentalange, et al. 2016. Mx1 reveals innate pathways to antiviral resistance and lethal influenza disease. *Science*. 352:463–466. https://doi.org/10.1126/science.aaf3926

Roberts, A., D. Deming, C.D. Paddock, A. Cheng, B. Yount, L. Vogel, B.D. Herman, T. Sheahan, M. Heise, G.L. Genrich, et al. 2007. A mouse-adapted SARS-coronavirus causes disease and mortality in BALB/c mice. *PLoS Pathog*. 3. e5. https://doi.org/10.1371/journal.ppat.0030005

Rockx, B., T. Kuiken, S. Herfst, T. Bestebroer, M.M. Lamers, B.B. Oude Munnink, D. de Meulder, G. van Amerongen, J. van den Brand, N.M.A. Okba, et al. 2020. Comparative pathogenesis of COVID-19, MERS, and SARS in a nonhuman primate model. *Science*. 368:1012–1015. https://doi.org/10.1126/science.abb7314

Seo, S.U., H.J. Kwon, H.J. Ko, Y.H. Byun, B.L. Seong, S. Uematsu, S. Akira, and M.N. Kweon. 2011. Type I interferon signaling regulates Ly6C(hi) monocytes and neutrophils during acute viral pneumonia in mice. *PLoS Pathog*. 7. e1001304. https://doi.org/10.1371/journal.ppat.1001304

Sia, S.F., L.M. Yan, A.W.H. Chin, K. Fung, K.T. Choy, A.Y.L. Wong, P. Kaewpreedee, R.A.P.M. Perera, L.L.M. Poon, J.M. Nicholls, et al. 2020. Pathogenesis and transmission of SARS-CoV-2 in golden hamsters. *Nature*. https://doi.org/10.1038/s41586-020-2342-5

Stadlbauer, D., F. Amanat, V. Chromikova, K. Jiang, S. Strohmeier, G.A. Arunkumar, J. Tan, D. Bhavsar, C. Capuano, E. Kirkpatrick, et al. 2020. SARS-CoV-2 Seroconversion in Humans: A Detailed Protocol for a Serological Assay, Antigen Production, and Test Setup. *Curr. Protoc. Microbiol.* 57. e100. https://doi.org/10.1002/cpmc.100

Sun, J., Z. Zhuang, J. Zheng, K. Li, R.L. Wong, D. Liu, J. Huang, J. He, A. Zhu, J. Zhao, et al. 2020. Generation of a Broadly Useful Model for COVID-19 Pathogenesis, Vaccination, and Treatment. *Cell*. S0092-8674(20)30741-8. https://doi.org/10.1016/j.cell.2020.06.010

tenOever, B.R.. 2016. The Evolution of Antiviral Defense Systems. *Cell Host Microbe*. 19:142–149. https://doi.org/10.1016/j.chom.2016.01.006

Wang, D., B. Hu, C. Hu, F. Zhu, X. Liu, J. Zhang, B. Wang, H. Xiang, Z. Cheng, Y. Xiong, et al. 2020. Clinical Characteristics of 138 Hospitalized Patients With 2019 Novel Coronavirus-Infected Pneumonia in Wuhan, China. *JAMA*. 323:1061. https://doi.org/10.1001/jama.2020.1585

Yockey, L.J., K.A. Jurado, N. Arora, A. Millet, T. Rakib, K.M. Milano, A.K. Hastings, E. Fikrig, Y. Kong, T.L. Horvath, et al. 2018. Type I interferons instigate fetal demise after Zika virus infection. *Sci. Immunol*. 3. eaao1680. https://doi.org/10.1126/sciimmunol.aao1680

Zhao, J., K. Li, C. Wohlford-Lenane, S.S. Agnihothram, C. Fett, J. Zhao, M.J. Gale, Jr., R.S. Baric, L. Enjuanes, T. Gallagher, et al. 2014. Rapid generation of a mouse model for Middle East respiratory syndrome. *Proc. Natl. Acad. Sci. USA*. 111:4970–4975. https://doi.org/10.1073/pnas.1323279111

Zhou, Z., L. Ren, L. Zhang, J. Zhong, Y. Xiao, Z. Jia, L. Guo, J. Yang, C. Wang, S. Jiang, et al. 2020. Heightened Innate Immune Responses in the Respiratory Tract of COVID-19 Patients. *Cell Host Microbe*. 27:883–890.e2. https://doi.org/10.1016/j.chom.2020.04.017

Zhu, N., D. Zhang, W. Wang, X. Li, B. Yang, J. Song, X. Zhao, B. Huang, W. Shi, R. Lu, et al; China Novel Coronavirus Investigating and Research Team. 2020. A Novel Coronavirus from Patients with Pneumonia in China, 2019. *N. Engl. J. Med*. 382:727–733. https://doi.org/10.1056/NEJMoa2001017

Supplemental material

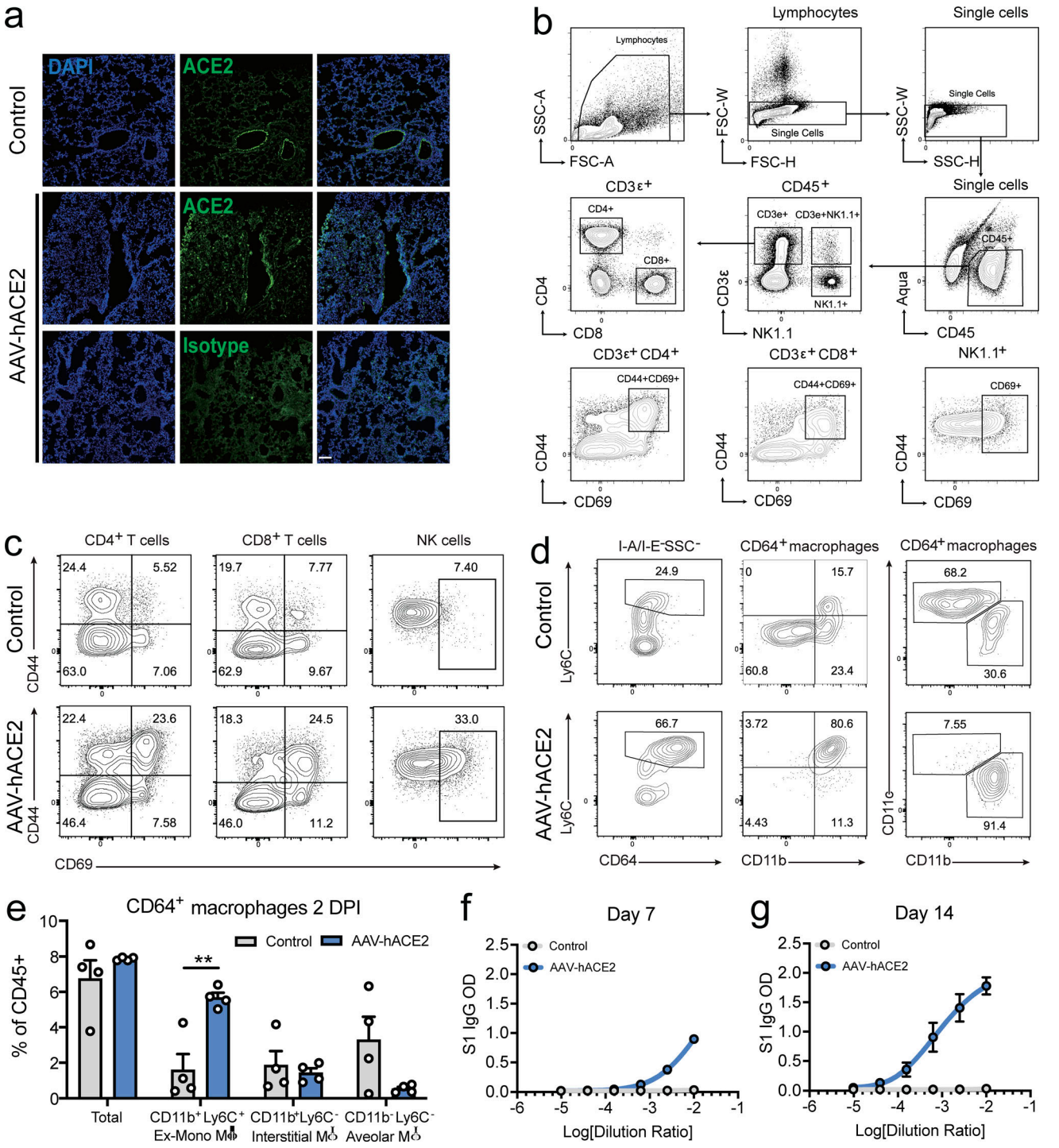

Figure S1. **AAV-hACE2 infection makes WT mice susceptible to SARS-CoV-2. (a)** Immunofluorescence staining of ACE2 in mice transduced with AAV-hACE2, 20 d after transduction. **(b)** Flow cytometry gating strategy for Fig. 1 g; Fig. 3, g–i; Fig S1 c; and Fig S3, a–c. **(c)** Representative flow cytometry plots for Fig. 1 g T cells and NK cells. **(d)** Representative flow cytometry plots for Fig. 1 g myeloid cells. **(e)** Different macrophage populations in the lungs of SARS-CoV-2–infected control (AAV-GFP or Mock) or AAV-hACE2 mice 2 DPI by flow cytometry. Data are pooled from two independent experiments, $n = 4$ mice per group, and are represented as mean ± SEM. P values were calculated by two-tailed unpaired Student's t test. **, $P < 0.01$. **(f)** Sera of mice were collected 7 DPI with SARS-CoV-2, and limiting dilutions were made to measure reactivity against S1 protein of SARS-CoV-2 using ELISA. **(g)** Sera of mice were collected 14 DPI with SARS-CoV-2, and limiting dilutions were made to measure reactivity against S1 protein of SARS-CoV-2 using ELISA. Scale bar, 100 µm. FSC-A, forward scatter area; FSC-H, forward scatter height; FSC-W, forward scatter width; SSC-A, side scatter area; SSC-H, side scatter height; SSC-W, side scatter width.

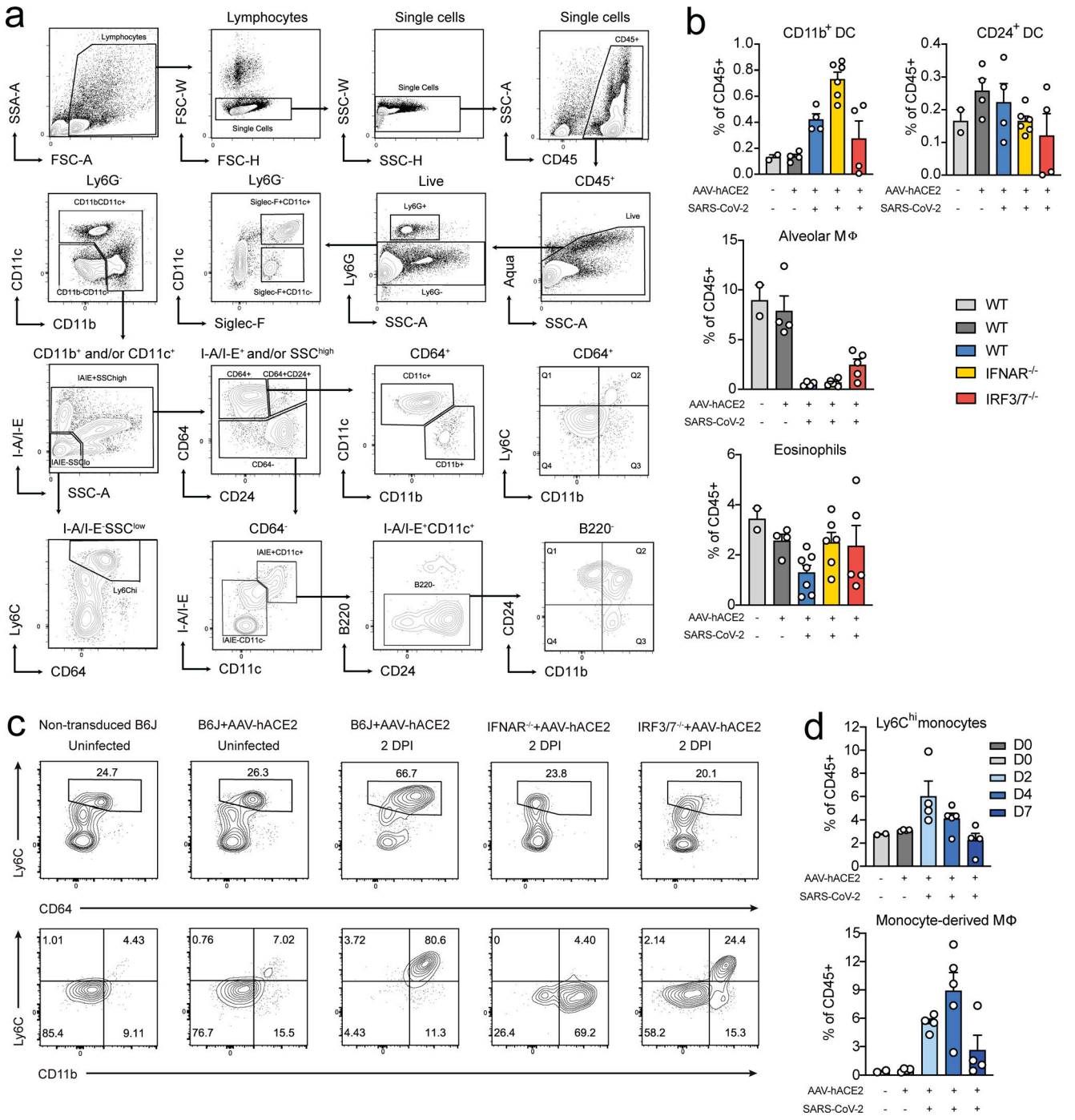

Figure S2. **Myeloid cell infiltration in SARS-CoV-2–infected mice. (a)** Flow cytometry gating strategy for Fig. 1 g; Fig. 3, d–f; Fig S1, b and e; and Fig. S2, b–d. **(b)** Relative percentage of different cell populations in indicated knockout mice infected with SARS-CoV-2 2 DPI (WT [light gray] nontransduced, noninfected values from single experiment, *n* = 2; WT [dark gray] AAV-hACE2 and not infected values from two independent experiments, *n* = 4; WT [blue] AAV-hACE2 and infected values from two independent experiments, *n* = 4; IFNAR$^{-/-}$ values from three independent experiments, *n* = 6; and IRF3/7$^{-/-}$ values from two independent experiments, *n* = 5. **(c)** Representative flow cytometry plots for Fig. 3, d and e. **(d)** Relative percentage of myeloid cell populations in WT mice transduced with AAV-hACE2 at 2, 4, and 7 d after SARS-CoV-2 infection (WT [light gray] nontransduced, noninfected values from single experiment, *n* = 2; WT [dark gray] AAV-hACE2 and not infected values from two independent experiments, *n* = 4; WT [blue] AAV-hACE2 and infected values from two independent experiments, *n* = 4, at each time point. FSC-A, forward scatter area; FSC-H, forward scatter height; FSC-W, forward scatter width; SSC-A, side scatter area; SSC-H, side scatter height; SSC-W, side scatter width.

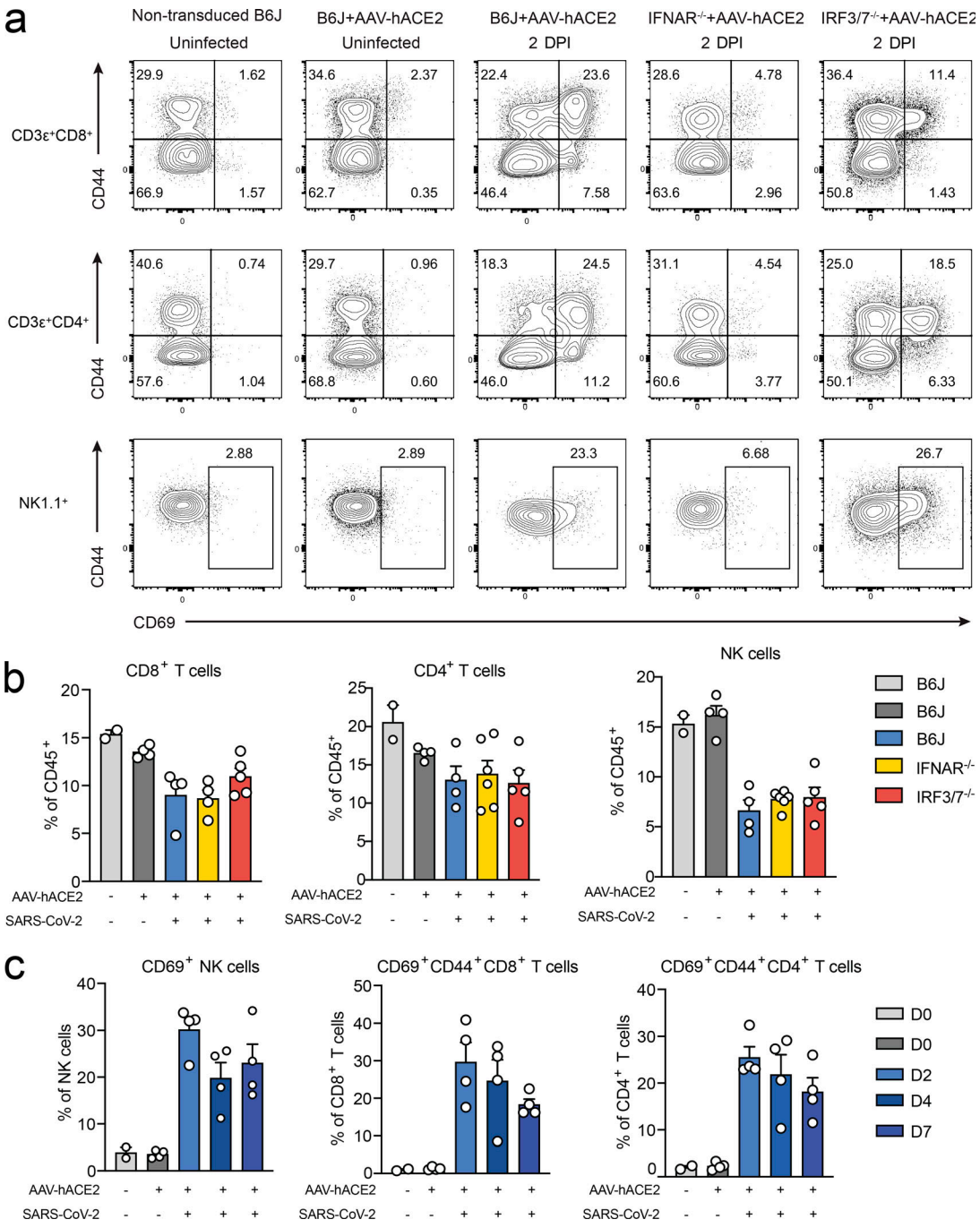

Figure S3. **T cell and NK cell infiltration in SARS-CoV-2–infected mice. (a)** Representative flow cytometry plots for Fig. 3, g–i. **(b)** Relative percentage of different lymphoid cell populations in different knockout mice infected with SARS-CoV-2 2 DPI (WT [light gray] nontransduced, noninfected values from single experiment, *n* = 2; WT [dark gray] AAV-hACE2 and not infected values from two independent experiments, *n* = 4; WT [blue] AAV-hACE2 and infected values from two independent experiments, *n* = 4; IFNAR$^{-/-}$ values from three independent experiments, *n* = 6; and IRF3/7$^{-/-}$ values from two independent experiments, *n* = 5). **(c)** Relative percentage of lymphoid cell populations in WT mice transduced with AAV-hACE2 at 2, 4, and 7 d after SARS-CoV-2 infection (WT [light gray] nontransduced, noninfected values from single experiment, *n* = 2; WT [dark gray] AAV-hACE2 and not infected values from two independent experiments, *n* = 4; WT [blue] AAV-hACE2 and infected values from two independent experiments, *n* = 4, at each time point).